coatings

MDPI

Article

Cutting Performance of a Longitudinal and Torsional Ultrasonic Vibration Tool in Milling of Inconel 718

Hang Zhang [1,2], Guosheng Su [1,2,*], Yan Xia [1,2,*], Peirong Zhang [1,2], Binxun Li [1,2], Yujing Sun [1,2], Jin Du [1,2] and Bin Fang [1,2]

[1] School of Mechanical Engineering, Qilu University of Technology (Shandong Academy of Sciences), Jinan 250353, China
[2] Shandong Institute of Mechanical Design and Research, Jinan 250031, China
* Correspondence: sgs@qlu.edu.cn or suguosheng@sina.com (G.S.); yxia1220@foxmail.com (Y.X.)

Abstract: Inconel 718 has excellent thermal and chemical properties and is widely used in the manufacture of aerospace parts; however, there are some problems in the machining of Inconel 718, such as a large milling force, serious tool wear, and poor surface quality. In this research, a type of longitudinal–torsional ultrasonic milling (LTUM) tool is designed based on theoretical computations and FEM simulation analysis. To verify the design rationality of the developed LTUM tool, milling experiments are performed. It is verified that the LTUM tool can realize an elliptical vibration path at the tool tip. The resonance frequency of the tool is 21.32 kHz, the longitudinal amplitude is 6.8 μm, and the torsional amplitude is 1.4 μm. In the milling of Inconel 718, the experimental data of LTUM are compared with those of conventional milling (CM). The comparative experiments show that the LTUM tool can effectively lessen the milling force and tool wear in the milling of Inconel 718, improve the surface quality, inhibit the generation of burrs, and improve the chip breaking ability. The application potential of the LTUM tool in high-performance milling of Inconel 718 parts is proven.

Keywords: ultrasonic vibration; ultrasonic assisted vibration milling; milling tool design

check for updates

Citation: Zhang, H.; Su, G.; Xia, Y.; Zhang, P.; Li, B.; Sun, Y.; Du, J.; Fang, B. Cutting Performance of a Longitudinal and Torsional Ultrasonic Vibration Tool in Milling of Inconel 718. *Coatings* **2024**, *14*, 719. https://doi.org/10.3390/coatings14060719

Academic Editors: Ben Beake and Giorgos Skordaris

Received: 17 April 2024
Revised: 21 May 2024
Accepted: 30 May 2024
Published: 5 June 2024

Copyright: © 2024 by the authors. Licensee MDPI, Basel, Switzerland. This article is an open access article distributed under the terms and conditions of the Creative Commons Attribution (CC BY) license (https://creativecommons.org/licenses/by/4.0/).

1. Introduction

Inconel 718 has excellent properties such as high temperature resistance, oxidation resistance, and corrosion resistance. It is commonly used in aerospace parts manufacturing, but its cutting performance is poor. In the cutting process, it has the characteristics of a large milling force [1], serious tool wear, and poor surface quality. With the development of the aerospace field, the cutting performance and surface quality of Inconel 718 are increasingly demanded. Therefore, it is an urgent problem to explore ways to improve the cutting performance and surface quality of Inconel 718.

Ultrasonic vibration machining is a machining method that applies ultrasonic waves to a cutting tool in a regular manner, allowing the tool to perform ultrasonic frequency vibration in a special direction and mode. Ultrasonic vibration machining is widely used in the fields of grinding [2,3], boring [4], surface rolling [5,6], milling [7,8], drilling [9,10], and turning [11]. Compared with CM, ultrasonic vibration milling has many advantages, such as effectively improving the surface characteristics of parts [12] and residual stress, reducing tool wear [13], suppressing tool chatter, reducing the milling force [14,15], and extending tool life [16].

Most ultrasonic milling tools can be classified as one-dimensional ultrasonic vibration tools and two-dimensional ultrasonic vibration tools. In the field of one-dimensional ultrasonic vibration, Ni et al. [17] designed a one-dimensional longitudinal ultrasonic milling tool and conducted comparative milling experiments on Ti-6Al-4V for CM and ultrasonic milling. It was concluded that ultrasonic milling had significant effects on reducing the milling force, improving the surface quality, and suppressing burrs. Chen et al. [18] designed a one-dimensional longitudinal milling tool and compared the traditional helical

milling and ultrasonic helical milling of Ti-6Al-4V alloy. By analyzing the two processing techniques, it was concluded that the aperture error and surface roughness of the ultrasonic helical milling hole were smaller than those in helical milling, and the subsurface hardness and surface residual compressive stress of the processed hole were significantly improved. Chang et al. [19] proposed a one-dimensional longitudinal ultrasonic milling tool. CM and ultrasonic vibration milling experiments of GH4169 superalloy were carried out. The results showed that ultrasonic vibration milling could produce finer grains, higher residual stress, and reduce the occurrence of tool chatter. The milling force was significantly reduced, thereby improving the wear resistance, strength, and fatigue life of the material. Long et al. [20] designed an exponential horn based on a one-dimensional wave equation and equivalent circuit theory. After the addition of ultrasonic vibration, the tool could produce torsional vibration. The resonance frequency and torsional amplitude were measured, and the results showed that the measurement results were consistent with the theoretical results, providing a guiding role for the development of a torsional ultrasonic horn.

However, a one-dimensional ultrasonic milling tool only vibrates in the axial or tangential direction, while a two-dimensional ultrasonic milling tool can vibrate in the tangential and axial directions, forming a circular or elliptical motion trajectory so that its cutting effect is better than that of a one-dimensional ultrasonic milling tool.

The methods for producing the longitudinal–torsional vibration mode are as follows. A double excitation vibration device is adopted, that is, a tangentially polarized piezoelectric ceramic sheet and a longitudinal vibration piezoelectric ceramic sheet are designed to generate composite vibration. The principle of this method is to change the longitudinal vibration and the torsional vibration by changing the sound speed of the longitudinal vibration and the torsional vibration so that the transducer resonates at the same frequency in the longitudinal–torsional vibration. However, the manufacturing technology of a tangentially polarized piezoelectric ceramic sheet is not perfect, which makes it difficult to satisfy the demands of high-power processing, so it is not widely used. The second method is to use a single excitation vibration device by setting a modal conversion structure on the horn or transducer so that the single longitudinal vibration generated by the transducer is converted into longitudinal–torsional vibration. This method has the advantages of a simple structure and convenient use, and it overcomes the shortcomings of a double excitation vibration device.

In the field of two-dimensional ultrasonic vibration, Ma et al. [21] proposed a single-excitation LTUM tool that set a spiral slot structure on the conical surface of a horn to achieve longitudinal–torsional conversion. A surface roughness Ra of 0.5 μm was achieved in the milling of BK0 optical glass, and this process also showed great advantages in fast chip removal. However, the horn with a spiral slot structure had many parameters affecting frequency resonance, and the model was difficult to establish. Ying et al. [22] designed a single-excitation LTUM tool for titanium alloy milling. By designing spiral grooves on the conical surface of the horn to realize longitudinal and torsional transformation, the tool could improve the compressive stress and fatigue resistance design performance of titanium alloy, laying a foundation for the study of compressive stress and fatigue resistance of titanium alloy. However, the spiral groove structure was set at the conical end of the horn, which increased the spiral groove parameters and made design optimization more difficult. Geng et al. [23] proposed a dual-excitation ultrasonic milling tool for CFRP processing. Two sets of piezoelectric ceramic plates were used to generate bending vibration at the end of the tool. Compared with traditional grinding, the surface integrity of ultrasonic machining was better, and the tool life was increased by 1.98 times. The surface after traditional grinding exhibited fiber pull-out, irregular tool feed marks, and higher roughness. However, the use of two sets of piezoelectric ceramic plates in this tool greatly increased the manufacturing cost, and the design and processing process were complex. Zheng et al. [24] proposed a single-excitation oblique longitudinal–torsional ultrasonic milling tool, which realized longitudinal–torsional conversion by machining chutes on the milling tool. The rotation axis of the tool was slightly tilted, and the tilt angle was about

15 °, which could form a good microstructure surface morphology on the simulated aircraft wing and biomedical metal surface. The fish-scale microstructure was prepared on the curved surface structure of the implant. Compared with CM, it avoided the phenomenon of secondary back cutting. However, this ultrasonic tool required the design of a chute structure on the milling tool, which was difficult to manufacture, and the types of milling tools suitable for clamping were limited. Du et al. [25] developed an ultrasonic milling tool with longitudinal bending vibration mode. When the same voltage was applied, the PZT ceramics on the transducer became thicker and thinner respectively, thus forming bending vibration. The innovation of this tool is that it could achieve both an impact ironing effect and intermittent cutting effect at the same time, so as to achieve high-precision milling. Compared with traditional milling and one-dimensional longitudinal ultrasonic milling, this tool reduced the milling force by 85.2% and 54.5%, respectively, reduced the surface roughness, and effectively suppressed the generation of burrs. However, the tool was not innovative in structure.

Based on the above research, a single-excitation LTUM tool is designed, which is more compact. The chute is set at the cylindrical end, and the structure realizes longitudinal–torsional conversion. The structure is simple and easy to manufacture. First, the motion characteristics of LTUM are analyzed and designed. The single excitation ultrasonic horn is optimized with Abaqus finite element analysis software. Then, the impedance analysis experiment and amplitude test experiment are carried out on the designed LTUM tool to verify the performance parameters of the designed ultrasonic tool. Finally, milling experiments are carried out on the difficult-to-cut material Inconel 718. It is concluded that the LTUM tool can effectively reduce the milling force and tool wear, improve the surface quality, inhibit the generation of burrs, and improve the chip breaking ability when milling Inconel 718. The feasibility of the LTUM tool design is proven, which provides guidance for the development of LTUM tools and verifies that LTUM technology can significantly improve the machining performance of Inconel 718 material.

2. Design of LTUM Tool

2.1. Motion Characteristic Analysis of LTUM

LTUM couples the vibration of the torsional vibration along the rotation direction of a tool and the ultrasonic longitudinal vibration along the longitudinal direction of the tool, with the tool as the vibration carrier, and the ultrasonic vibration output is uniform and stable. Figure 1 shows the LTUM model. The tool cutting edge motion is composed of the tool rotation motion, ultrasonic longitudinal vibration, ultrasonic torsional vibration, and feed motion.

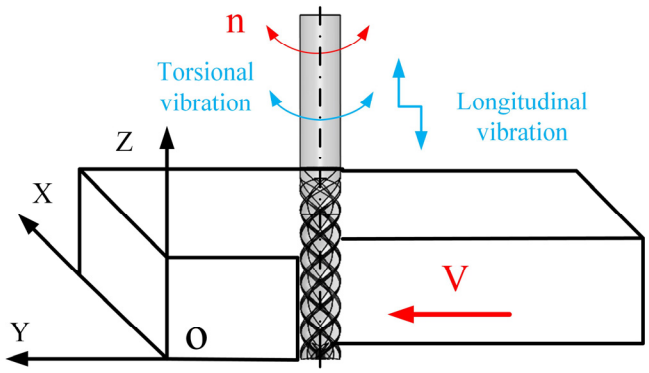


Figure 1. LTUM model.

When the tool is subjected to ultrasonic vibration for cutting, the motion path of the tool becomes very complicated. In ultrasonic milling, the trajectory of the cutting edge affects the machining efficiency and work efficiency. Therefore, it is necessary to establish

the trajectory equation of the milling edge. In the CM process, the trajectory equation of the milling edge is as follows:

$$\begin{cases} O(s) = m{\cdot}s + u{\cdot}\sin(2\pi ws/60) \\ P(s) = u{\cdot}\cos(2\pi ws/60) \\ Q(s) = 0 \end{cases} \quad (1)$$

LTUM is based on CM, and longitudinal–torsional vibration is applied to the tool at the same time. The path of motion equation of the milling edge is as follows:

$$\begin{cases} O(s) = m{\cdot}s + u{\cdot}\sin(2\pi ws/60 + e{\cdot}\cos(2\pi Ls + \theta_2)/u) \\ P(s) = u{\cdot}\cos(2\pi ws/60 + e{\cdot}\cos(2\pi Ls + \theta_2)/u) \\ Q(s) = d{\cdot}\sin(2\pi Ls + \theta_1) \end{cases} \quad (2)$$

where m is the feed rate, where $m = wszf_z/60$; w is the speed of the main spindle; f_z is the feed per tooth; L is the supersonic frequency; d is the ultrasonic longitudinal amplitude; e is the ultrasonic torsional amplitude; u is the tool radius; and θ_1 and θ_2 are the initial phases of ultrasonic longitudinal vibration and torsional vibration, respectively. Figure 2 shows their trajectories.

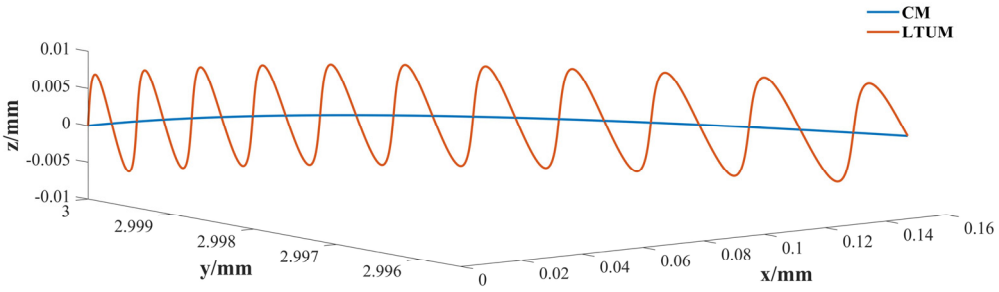


Figure 2. Tool cutting edge trajectories.

By comparing the cutting edge trajectories of CM and LTUM, the cutting edge trajectory of LTUM has a periodic fluctuation phenomenon. This is because LTUM generates periodic torsional vibration based on longitudinal vibration. This composite vibration leads to periodic contact and separation between the tool and the workpiece, so LTUM can produce intermittent cutting, while CM can only be processed continuously. LTUM can reduce the milling force and cutting heat, reduce the surface roughness, and improve the surface quality.

2.2. Design of Longitudinal-Torsional Ultrasonic Horn

The horn is an indispensable part of the whole LTUM tool; it has the functions of amplifying amplitude, matching impedance, and gathering energy [26]. The horn model is designed in an ideal state, so it is necessary to ensure that each part of the horn is made of uniform material and mechanical loss is not considered. When the wavelength of the horn is greater than the cross-section size, it can be considered that the longitudinal wave spreads along the longitudinal direction of the horn. The displacement and stress of the particle on the cross-section of the horn should be evenly distributed. For simple harmonic motion, each section of the horn should satisfy the fluctuating equation. The longitudinal vibration equation of the horn is as follows [27]:

$$\frac{\partial \xi}{\partial \xi} + \frac{1}{s} \times \frac{\partial s}{\partial y} \times \frac{\partial \xi}{\partial y} + k^2 \xi = 0 \quad (3)$$

where $s = s(x)$ is the cross-section area coefficient of the horn; $\xi = \xi(x)$ is the particle function; and $k = \omega/c$, where k is the circular wave number. ω is the angular frequency, c is the sound velocity, $c = (E/\rho)^{1/2}$, E is young's modulus, and ρ is the material density.

The stepped horn has a simple structure and an easy design and manufacturing process. The conical horn has the advantages of good stability, no stress concentration, and a large amplification coefficient [28]. The use of a conical composite stepped horn can also have the above advantages.

The large end of the horn should be connected to the transducer. Considering the diameter of the transducer, the diameter D of the large end of the horn is 30 mm and the diameter d of the small end is 15 mm.

The horn material is 20GrMnTi, and Table 1 shows the material properties. The design frequency f is 28 kHz, to facilitate the calculation, L_2 is set to 30 mm, and the design is shown in Figure 3. The large end L_1 is set to $\lambda/4$, and λ is the wavelength. The horn was designed using the four-terminal network method, and the specific design equation is as follows:

Area coefficient: $n = D/d$.

Circular wave number: $g = \omega/c = 2\pi f/c$.

Frequency equation:

$$\tan gL_3 = \frac{-(\sin gL_1 + \frac{\alpha}{g}\cos gL_1)(\cos gL_2 + \frac{\alpha}{g}n\sin gL_2) + \cos gL_1(\frac{\alpha}{g}n\cos gL_2 - \sin gL_2)}{-(\sin gL_1 + \frac{\alpha}{g}\cos gL_1)\sin gL_2 + \cos gL_1\cos gL_2} \quad (4)$$

where $n = D/d$ and $\alpha = (n-1)/nL_2$.

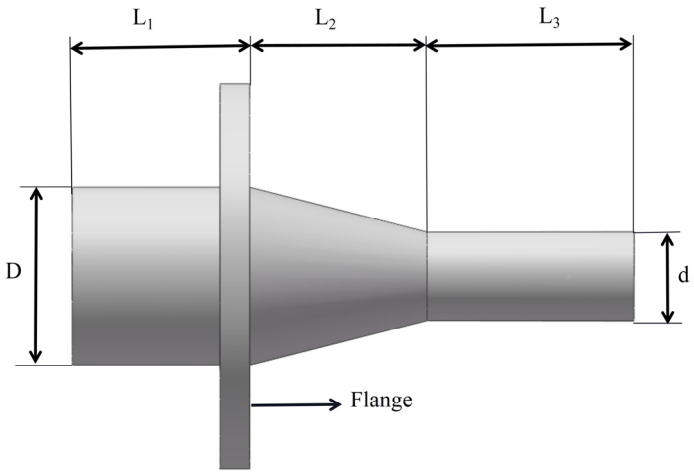


Figure 3. Conical horn.

Table 1. Material characteristics of the horn.

Material	Density (kg/m^3)	Elastic Modulus (GPa)	Poisson's Ratio σ
20GrMnTi	7800	207	0.3

The horn flange is set at the junction of the large end and the cone end, and the flange thickness is 5 mm.

The longitudinal wave loses a large amount of energy in the air. Ignoring the influence of secondary refraction, only the reflected longitudinal wave and the reflected shear wave are considered. Shear waves can easily cause shear deformation, and gas and liquid cannot bear the shear force, so the shear waves can only propagate in the solid state. As shown in Figure 4, the longitudinal wave is incident at an angle of α. When the longitudinal wave σ is reflected when it passes through the slanting slot position, a reflected longitudinal wave σ_1 with an angle of θ and a reflected transverse wave τ are generated. The reflected transverse wave vibrates along the circumferential direction of the horn to produce torsional vibration, and the reflected longitudinal wave vibrates along the axial direction of the horn to produce longitudinal vibration.

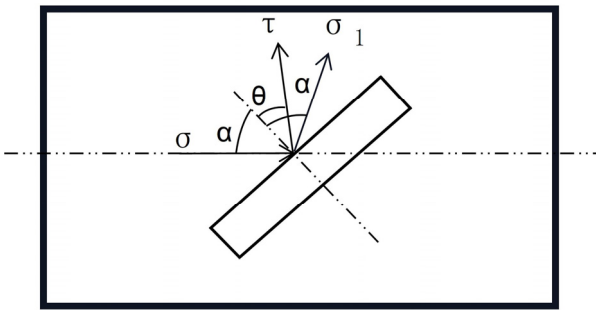


Figure 4. Principle of longitudinal-torsional conversion.

In summary, the slanting slot structure can make the longitudinal wave produce longitudinal–torsional waves and output these waves at the end of the horn. Figure 5 shows the structure of the horn: there are four slanting slots evenly distributed along the circumferential direction at the small end of the horn, with an angle of 60°, a length of 10 mm, a width of 3 mm, and a depth of 4.5 mm.

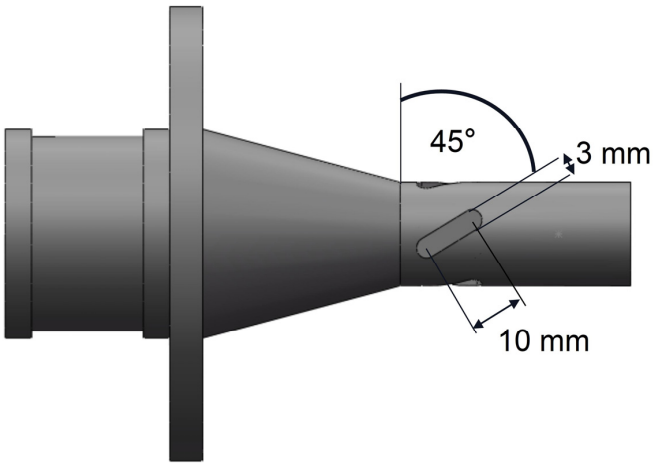


Figure 5. Slanting slot longitudinal–torsional horn.

2.3. FEM Analysis

The mode analysis of the horn was conducted with Abaqus software. Modal analysis is the basis of dynamic analysis, and the vibration characteristics of the workpiece can be determined by modal analysis. The three-dimensional model of the horn was imported into Abaqus software, and the fixed constraint was applied to the flange position of the horn. Figure 6 is the simulation result. When the 12th-order modal resonance frequency is 29,798 Hz, the horn could achieve longitudinal vibration, and the displacement vector of each point was the longitudinal displacement.

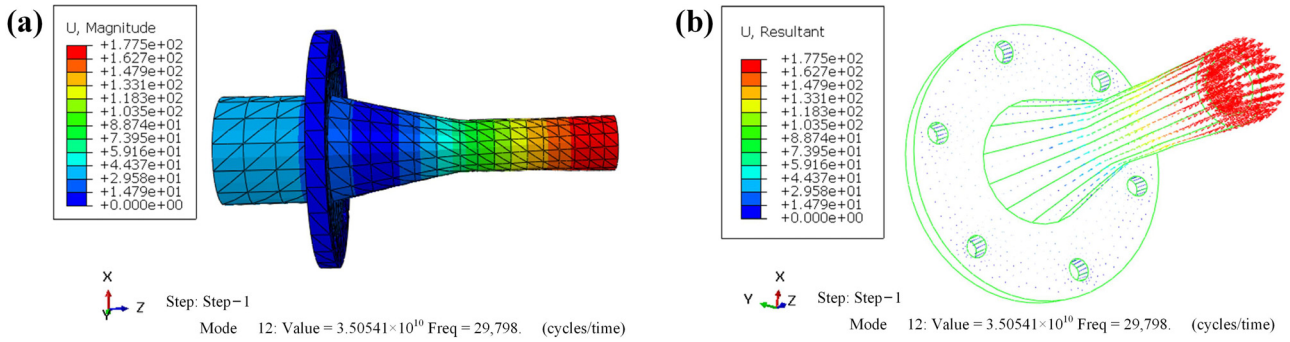


Figure 6. Modal analysis results of the longitudinal horn: (**a**) longitudinal horn vibration mode; (**b**) longitudinal horn vibration vector.

Figure 7 is the simulation result. At 28,133 Hz, the displacement vector at the end of the horn had a torsional trend. The horn generated longitudinal–torsional vibration, which met the design frequency requirements.

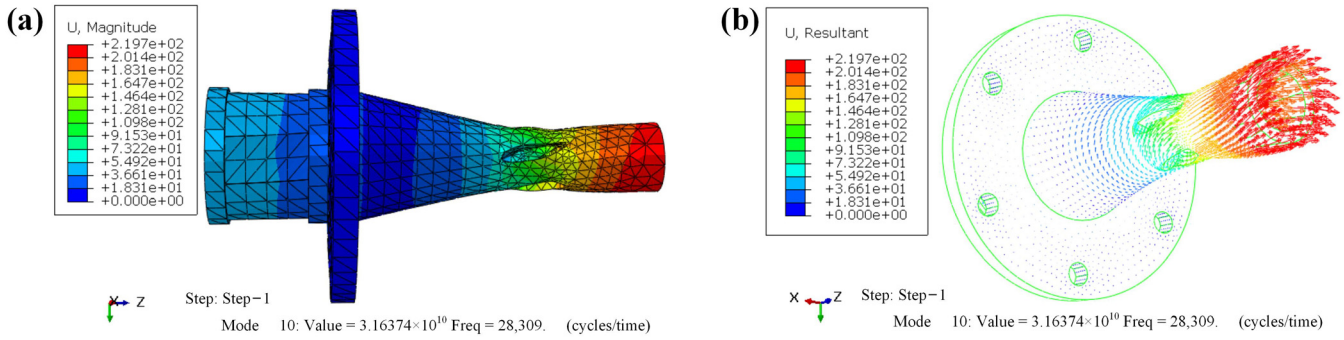


Figure 7. Modal analysis of the slanting slot longitudinal–torsional horn: (**a**) longitudinal–torsional horn vibration mode; (**b**) longitudinal–torsional horn vibration vector.

To ensure that the horn could efficiently transmit ultrasonic vibration to the tool during milling, a clamping method needed to be considered. The commonly used clamping methods are hot assembly connection and thread connection. The hot assembly connection structure is simple and the connection is tight, but it is not easy to disassemble and change the tool. Thread connection can reduce the loss of ultrasonic transmission, but processing is difficult and the cost is high. With comprehensive consideration, the spring chuck and the screw nut were used to connect the milling tool, as shown in Figure 8a. This connection method ensured the reliability of the clamping and the clamping of different straights. As shown in Figure 8b, after clamping the milling tool on the horn, the overall frequency reached 19,773 Hz.

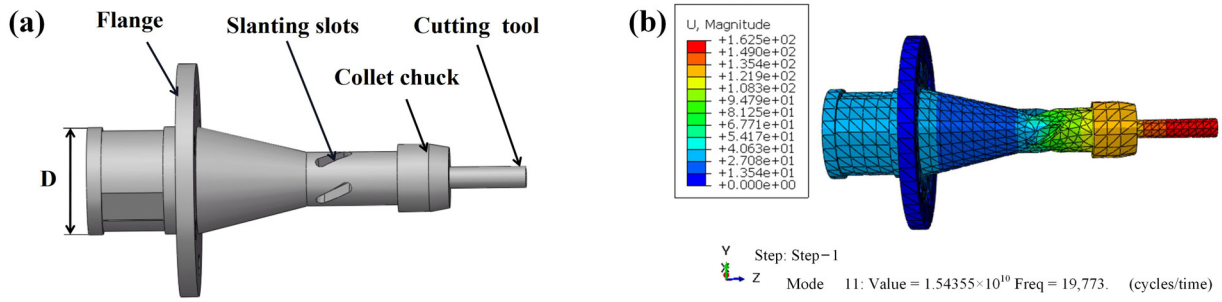


Figure 8. Analysis of ultrasonic milling tool: (**a**) ultrasonic milling tool assembly diagram; (**b**) ultrasonic milling tool modal analysis diagram.

Transient dynamic analysis is based on modal analysis to obtain the time of the tip output at a certain point at a fixed frequency. As shown in Figure 9a, a displacement excitation of 1 μm was applied to the large end cylinder of the horn, and the analysis frequency was 20–40 kHz. Transient dynamics analysis was carried out, and part of the outlet displacement curve was fitted. The vibration-cutting trajectory in three-dimensional space was obtained at the resonance frequency. At 21,042 Hz, the longitudinal vibration excitation y (t) = 0.001 × sin (2π × 21,042 × t) was applied to the large end of the horn to obtain the time displacement of the tool tip in the x-, y-, and z-directions. As shown in Figure 9a, the torsional amplitude was small, so it could be regarded as the bending amplitude in the y-direction.

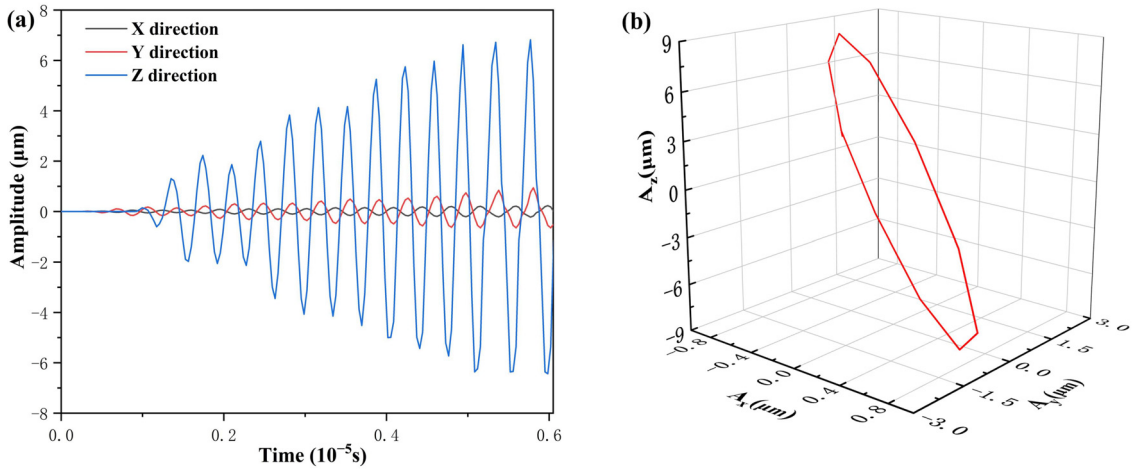


Figure 9. Dynamic response curves of the tool tip: (**a**) time–displacement curve; (**b**) three-dimensional elliptical trajectory.

The displacement in the x-, y-, and z-directions was combined to obtain a three-dimensional elliptical trajectory, as shown in Figure 9b. From the diagram, it can be seen that the elliptical trajectory synthesized by the tip in the x-, y-, and z-directions was regular, and the amplitudes were 6.9 μm and 1 μm.

2.4. Optimization of Ultrasonic Milling Tool

It can be seen from the discussion in the previous section that the parameters of the slanting slots affect the magnitude of the amplitude, that is, the torsional–longitudinal ratio of the torsional amplitude to the longitudinal amplitude. Additionally, the magnitude of the torsional–longitudinal ratio in the milling process determines the quality of the machined surface. To better match the horn to the 21 kHz transducer, some parameters of the horn needed to be optimized. The resonance frequency and torsional–longitudinal ratio of the horn affect the machining performance of the milling tool. The length of the small end of the horn and the parameters of the slanting slots affect the resonance frequency and torsional–longitudinal ratio. Through Abaqus simulation analysis, the end size and chute parameters of the horn were optimized, so that the frequency of the horn was closer to 21 kHz. At the small end of the horn, the slanting slots were evenly distributed along the axial direction. Considering the structure of the output end of the horn, the slanting slots were set to be 10 mm long, 3 mm wide, 4 mm deep, and 4 mm away from the connection between the cone and the small end. The slanting slot angle, slot depth, and the length of the small end of the horn were adjustable. The temporary slanting slot angle was 45°, the slot depth was 5 mm, and the length of the small end of the horn was 38 mm.

The single-factor method was used to change the length of the small end of the horn as well as the angle and depth of the slanting slots of the horn, and the parameters were kept unchanged. The resonance frequency of the horn at approximately 21 kHz was found, and the flange of the horn was guaranteed to be located at the node position. The changes in the resonance frequency f and the torsional–longitudinal ratio *e* of the horn are shown in Figure 10.

Figure 10a,b show the influences of the slanting slot angle on the resonance frequency and *e*. The resonance frequency *f* increased with the increase in the slanting slot angle, and the frequency was close to 21 kHz at approximately 55°. The ratio *e* first increased and then was reduced with the increase in the slanting slot angle, and the ratio reached the maximum at 55°. Figure 10c,d show the influences of the depth of the slanting slot on the resonance frequency *f* and *e*. The resonance frequency decreased slowly with the increase in the depth of the slanting slot, and when the slanting slot depth was approximately 5 mm, the resonance frequency *f* was close to 21 kHz. The ratio *e* increased as the depth of the slanting slot increased. Figure 10e,f show the influences of the L_3 length on the resonance

frequency f and e. Figure 10e shows the influence of L_3 on the resonance frequency. With the increase in the length of L_3, the resonance frequency f was reduced and was close to 21 k Hz at about 35 mm. Figure 10f shows the influence of L_3 on e. With the increase in L_3 length, e first increased and then was reduced, reaching the maximum at about 35 mm. Therefore, considering the resonance frequency f and e, the slanting slot parameters were set to be 10 mm long, 3 mm wide, and 4 mm deep.

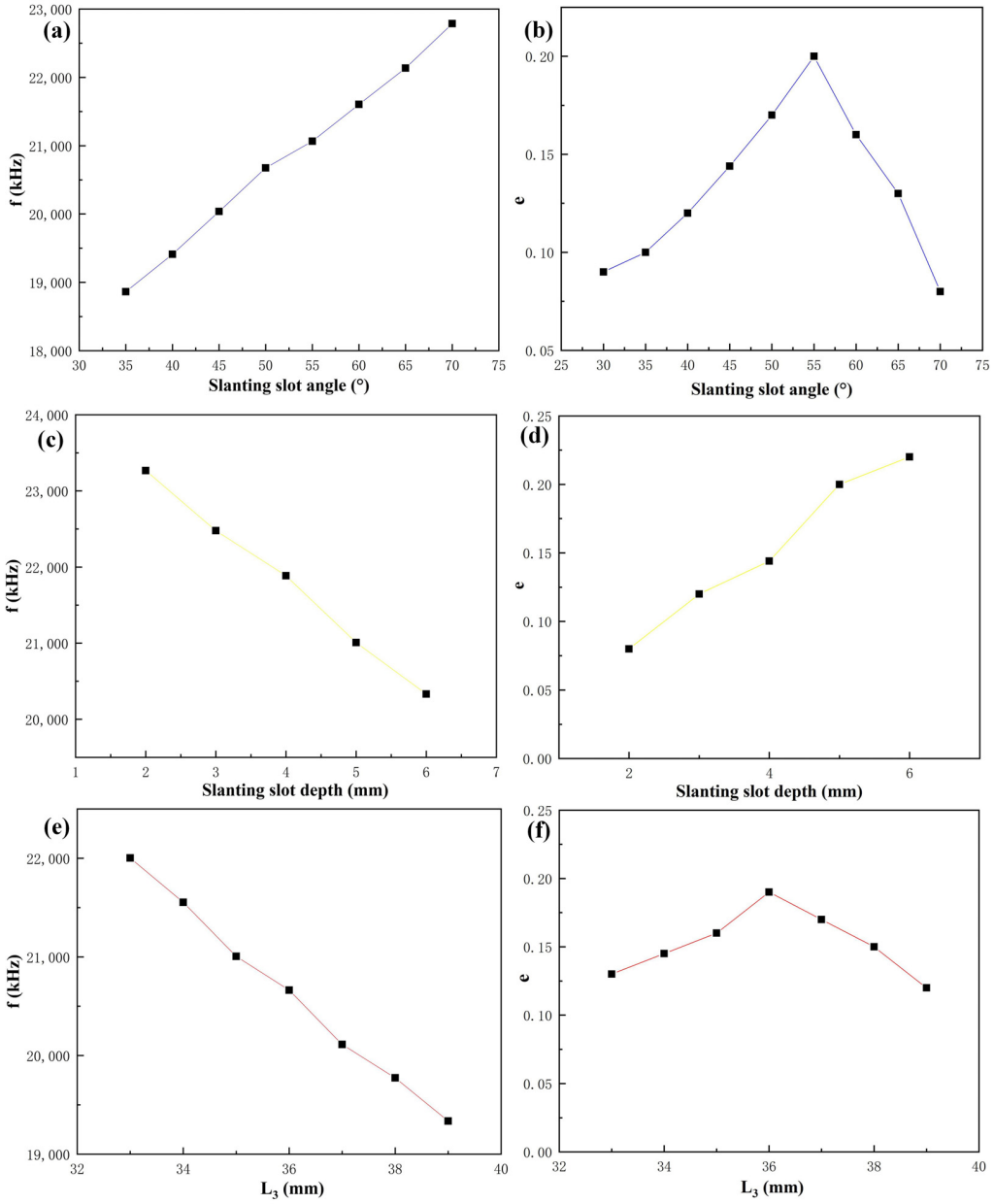


Figure 10. Influence of single factor horn parameters on the frequency f and torsional–longitudinal ratio e: (**a**) influence of the slanting slot angle on the resonance frequency f; (**b**) influence of the slanting slot angle on e; (**c**) influence of the slanting slot depth on the resonance frequency f; (**d**) influence of the chute depth on e; (**e**) influence of the L_3 length on the resonance frequency f; (**f**) influence of the L_3 length on e.

3. LTUM Tool Performance Test

According to the theoretical computation and finite element simulation analysis, a skewed longitudinal–torsional horn was designed. The transducer was connected to the large end of the longitudinal–torsional horn to form a longitudinal–torsional ultrasonic

vibrator. The longitudinal–torsional composite ultrasonic vibrator was installed inside the self-designed BT40 tool holder through six bolts. The electromagnetic induction device was fixed on the outside of the BT40 tool holder, and the LTUM tool was finally formed by connecting the wire with the transducer poles, as shown in Figure 11.

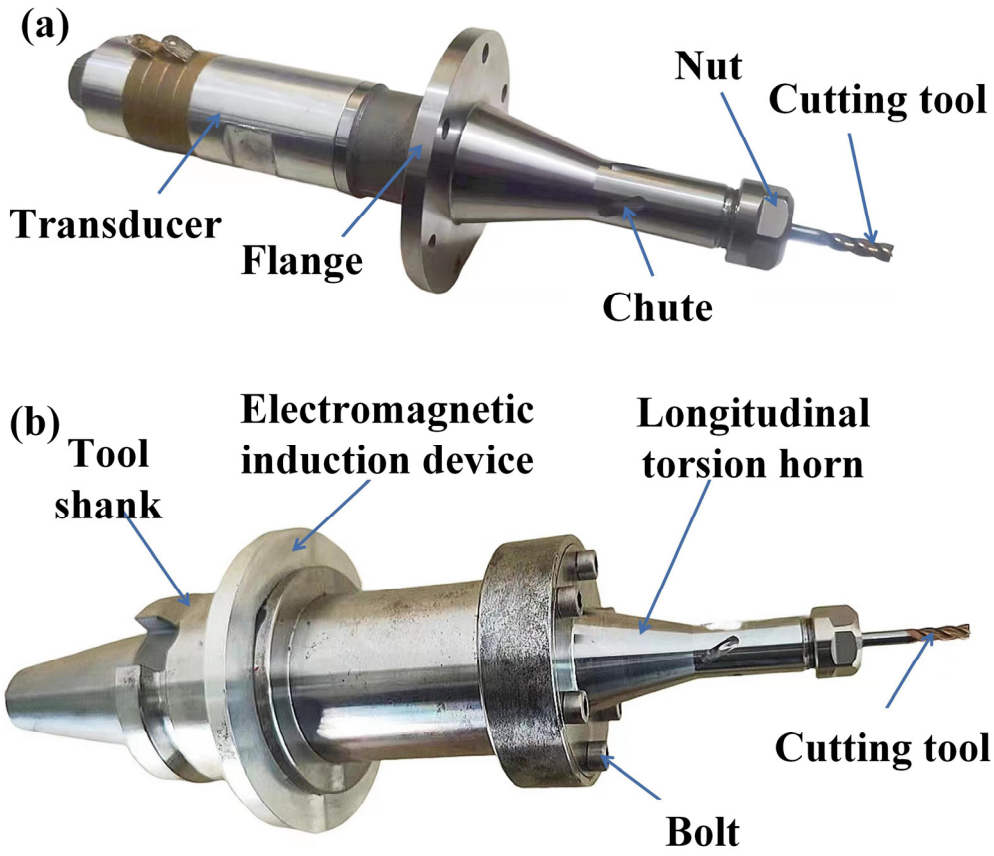


Figure 11. Object pictures: (**a**) longitudinal–torsional ultrasonic vibrator; (**b**) LTUM tool.

3.1. Impedance Analysis

In order to match the power of the ultrasonic power supply with the LTUM tool, impedance analysis of the tool was carried out. Impedance analysis can accurately measure the impedance of the tool and determine whether it is in good working condition.

The resonance frequency of the LTUM tool was measured using an impedance analyzer. The parameters of impedance analysis were set as follows: the initial frequency of the impedance analysis was 15 k Hz, and the termination frequency was 24.5 k Hz. Table 2 shows the main parameters of the impedance analysis. Figure 12 shows the impedance characteristic test results.

Table 2. Main parameters obtained by the impedance analyzer.

Parameter	Numerical Value (Unit)	Parameter	Numerical Value (Unit)
Resonance frequency F_s	21.32 kHz	Half power point F_2	21.33 kHz
Anti-resonance frequency F_p	21.46 kHz	Dynamic resistor R_1	107 Ω
Half power point F_1	21.31 kHz	Dynamic capacitance C_1	0.07 nF

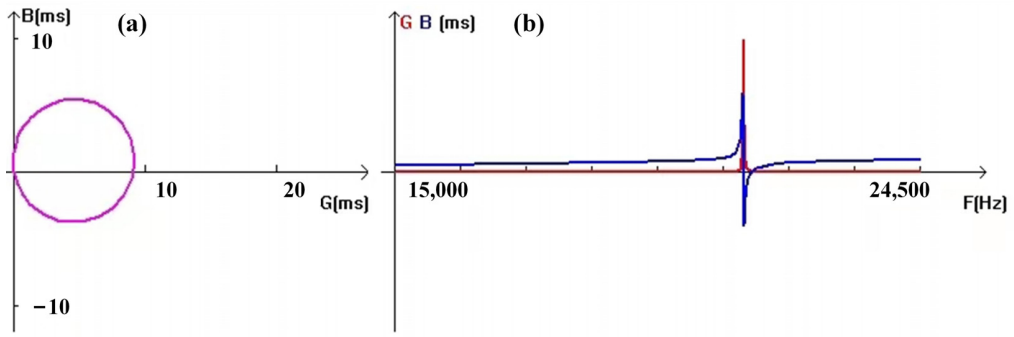


Figure 12. Impedance curves: (**a**) mobility circle; (**b**) G-B trajectories.

Figure 12a shows the admittance circle diagram of the LTUM tool. The admittance circle diagram reflects the resonance point and the surrounding characteristic curve. When there is no other circle in the conductance circle, the circle is better. The admittance curve was normal, indicating that the tool could work normally. Figure 12b shows the trajectory of conductance G and susceptance B with the change in frequency, where the blue line represents the susceptance curve of the LTUM tool near the resonance frequency and the red line represents the conductance curve near the resonance frequency. The admittance value of the frequency point near the resonance frequency fluctuated greatly, the peak value of the conductance G curve was narrow, and the conductance value of the other frequency points changed more gently. The resonance frequency of the LTUM tool corresponding to the peak value of the curve was 21,325 Hz. Compared with the simulated resonance frequency, the relative error of 21,042 Hz was only 0.013. The reason for the error was that the material properties defined by the finite element simulation were uniform, while the actual material was non-uniform due to manufacturing and assembly errors. In summary, it was proven that the LTUM tool was well designed, and the effectiveness of the finite element simulation was illustrated.

3.2. Amplitude Test Experiment

In the ultrasonic milling experiment, the size of the ultrasonic amplitude determines the quality of the surface. Therefore, the amplitude measurement experiment of the LTUM tool was carried out to test the ultrasonic amplitude of the cutter tip in the ideal state. Figure 13 shows the amplitude test diagram of the LTUM tool. The amplitude measurement device used in this experiment was a Doppler laser vibrometer. Because the torsional amplitude was small and difficult to measure, its arc length was approximately equal to its chord length, so the torsional amplitude was approximately equal to the bending amplitude in the Y-direction. The two displacement sensors A and B of the laser controller were vertically distributed in the Y- and Z-directions of the ultrasonic milling cutter, respectively, and the longitudinal amplitude (Z-direction) and torsional amplitude (Y-direction) were measured simultaneously.

The longitudinal amplitude and torsional amplitude were measured and processed by the laser controller and displayed on the computer display, as shown in Figure 14, which illustrates the amplitude curve of the tool tip in the Y-direction and the Z-direction. The longitudinal amplitude of the tool tip was 6.8 μm and the torsional amplitude was 1.4 μm. By combining the amplitudes of the Y- and Z-directions, the elliptical trajectory of Figure 15 was obtained.

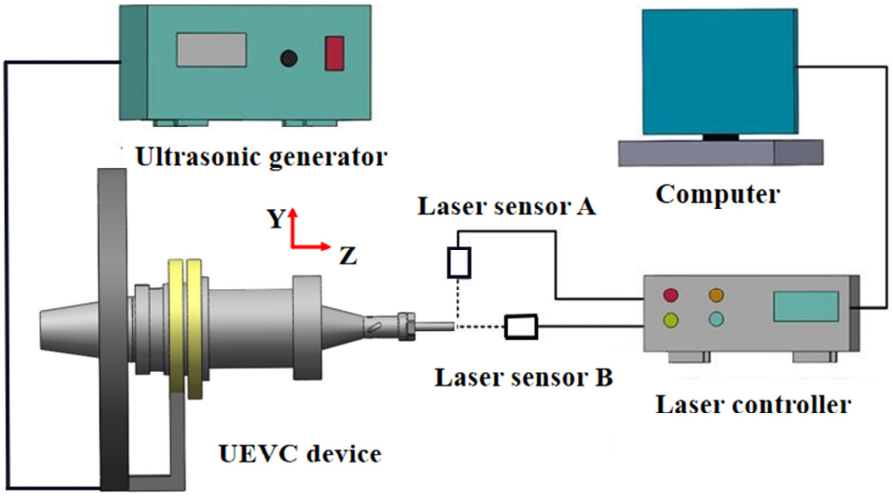


Figure 13. Schematic diagram of amplitude test of LTUM tool.

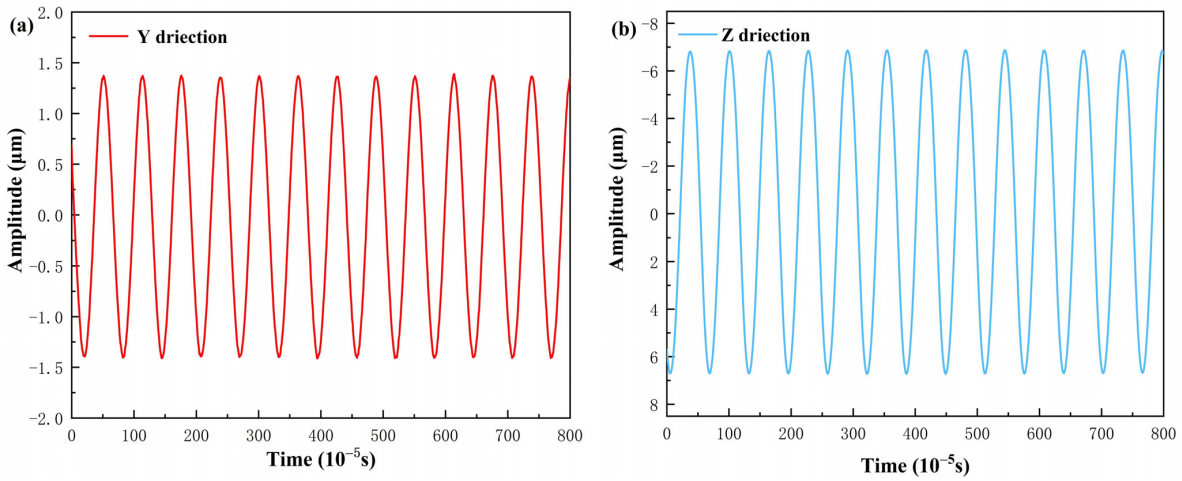


Figure 14. Amplitude test results: (**a**) *y*-axis (torsional amplitude); (**b**) *z*-axis (longitudinal amplitude).

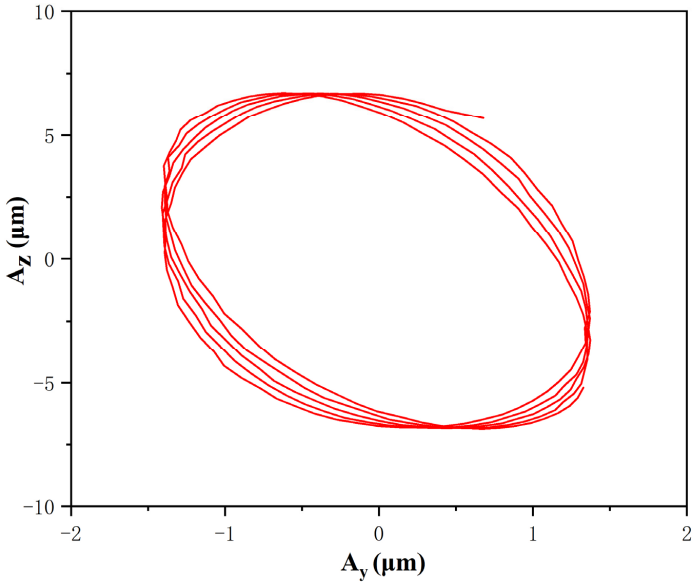


Figure 15. Synthetic elliptic motion trajectories in Y- and Z-directions.

4. Milling Experiments and Results

4.1. Experimental Design of LTUM

Milling experiments were performed using the designed LTUM tool to evaluate the cutting performance of the tool. The LTUM tool was installed on the DNM415 CNC milling machine, and the milling experiment of Inconel 718 was carried out, as shown in Figure 16. The three-dimensional milling force dynamometer produced by the Swiss company was used to measure the milling force, and the Inconel 718 workpiece was clamped on the dynamometer by fastening bolts. The Inconel 718 workpiece was 70 mm long, 35 mm wide, and 95 mm high. Table 3 shows the chemical constituents, and Table 4 shows the mechanical properties. A cemented carbide-coated milling cutter with high hardness, high compressive strength, good thermal conductivity, and wear resistance was selected. The overall tool was a four-tooth end milling tool, the tool length was 15 mm, the tool diameter was 6 mm, and the cutting method was side milling. This experimental platform laboratory had a constant temperature and constant humidity and was dustproof and shockproof. The stability of the entire Inconel 718 milling process and the stability of the test data were guaranteed. The milling experiment was carried out with and without ultrasonic vibration using the same parameters. The experimental parameters of side milling are shown in Table 5, and the experimental parameters of slot milling are shown in Table 6.

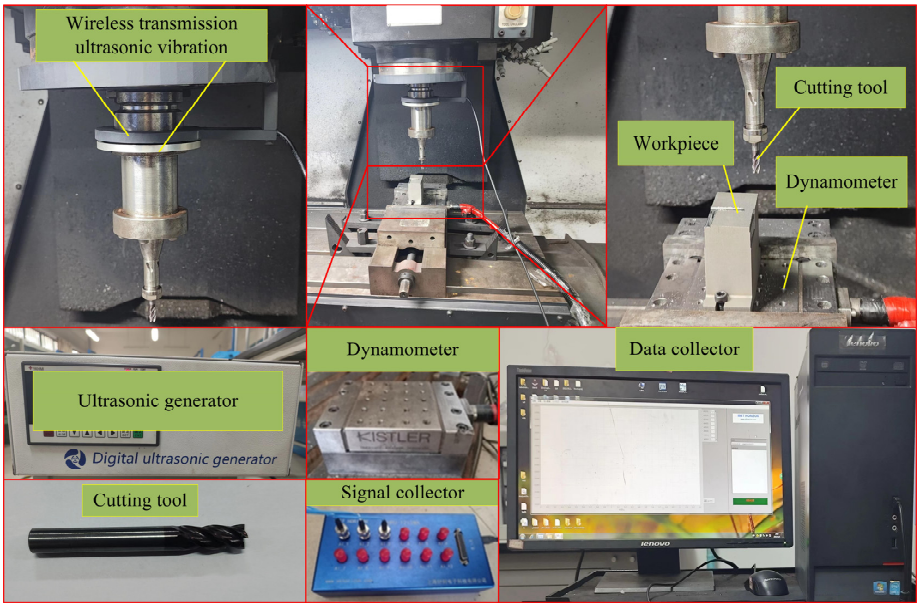


Figure 16. LTUM device.

Table 3. Chemical composition of Inconel 718.

C	Mn	Si	P	S	Gr	Ni	Co	Ri	Fe	Al
0.04	0.08	0.08	<0.015	0.002	18.37	53.37	0.23	0.98	1.78	0.50

Table 4. Mechanical properties of Inconel 718.

Property	Value
Density (kg/m^3)	8220
Elastic modulus (GPa)	210
Hardness (HV)	390
Poisson's ratio	0.3
Yield strength (MPa)	955
Tensile strength (MPa)	1150

Table 5. Side milling experimental parameters.

Parameters	Specifications	
	CM	**LTUM**
Speed of main spindle (r/min)	1000, 1500, 2000	1000, 1500, 2000
Feed speed (m/min)	100, 150, 200	100, 150, 200
Feed per tooth (mm/z)	0.025, 0.0375, 0.05	0.025, 0.0375, 0.05
Radial cutting depth (mm)	1, 2, 3	1, 2, 3
Axial cutting depth (mm)	5	5
Frequency (kHz)	-	21,000
Alon (μm)	0	6.8
Ator (μm)	0	1.4

Table 6. Slot milling experimental parameters.

Parameters	Specifications	
	CM	**LTUM**
Speed of main spindle (r/min)	1000, 1500, 2000	1000, 1500, 2000
Feed speed (m/min)	100, 150, 200	100, 150, 200
Feed per tooth (mm/z)	0.025	0.025
Cutting depth (mm)	1, 2, 3	1, 2, 3
Frequency (kHz)	-	21,000
Alon (μm)	0	6.8
Ator (μm)	0	1.4

4.2. Effect of LTUM on Surface Quality and Cutting Performance

Figure 17 shows the side milling surface under the two processing methods when the speed of the main spindle is 1000 r/min, the feed speed is 100 m/min, the radial depth of cutting is 2 mm, and the axial depth of cutting is 5 mm. The surface gloss of LTUM was poor. This was because the machined surface of LTUM was a pit formed by the ultrasonic elliptical cutting trajectory, and its gloss was poor after the diffuse reflection of light. Comparing the cutting surfaces under the two processing methods, it could be seen that the surface of the CM process produced irregular scales. After adding longitudinal–torsional ultrasonic vibration, the tool had high-frequency torsional vibration, which had an ironing effect on the machined surface and improved the surface quality.

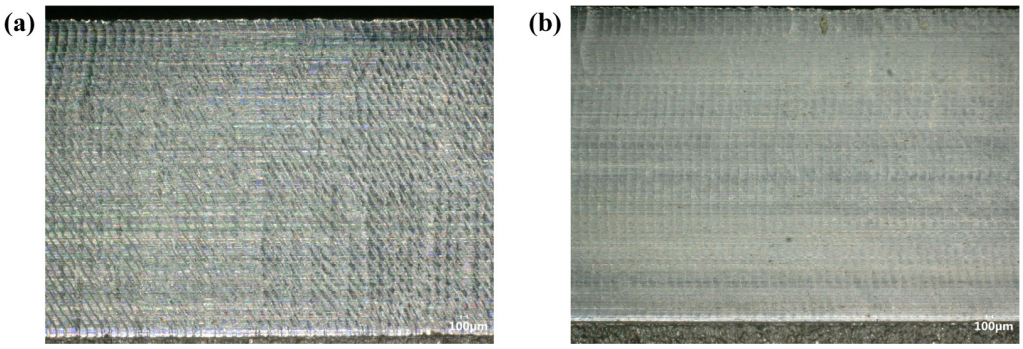


Figure 17. Side milling surface: (**a**) CM; (**b**) LTUM.

Figures 18 and 19 show the side milling surface morphologies observed by a super depth-of-field three-dimensional microscope (the speed of the main spindle is 1000 r/min, the feed speed is 100 m/min, the radial depth of cutting is 2 mm, and the axial depth of cutting is 5 mm). Figure 18 shows the surface micro-topography under CM processing. The machined surface was uneven, resulting in irregular gullies, which greatly reduced the surface quality. Figure 19 shows the surface morphology under longitudinal–torsional ultrasonic vibration. After longitudinal–torsional ultrasonic vibration was added, the

machined surface produced regular patterns and formed regular pit-like micro-textures, and the machined surface morphology was significantly improved. This was due to superposition of ultrasonic vibration, after which the tool tip trajectory changed from the traditional linear trajectory to the periodic fluctuation trajectory, which greatly improved the surface morphology and the machined surface quality. This result was consistent with the analysis of the cutting edge trajectory discussed in Section 2.1.

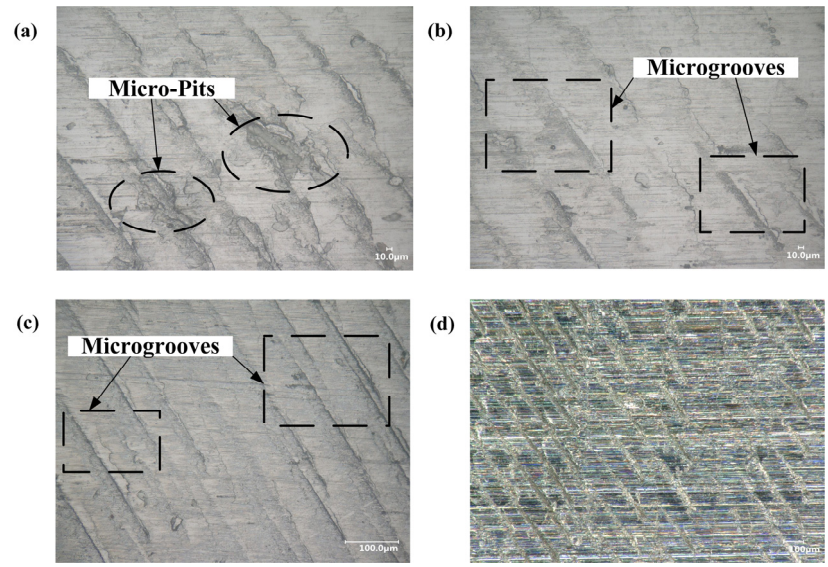


Figure 18. Side milling surface microstructure of CM: (**a**–**c**) Surface morphology under high magnification microscope; (**d**) Surface morphology under a low magnification microscope.

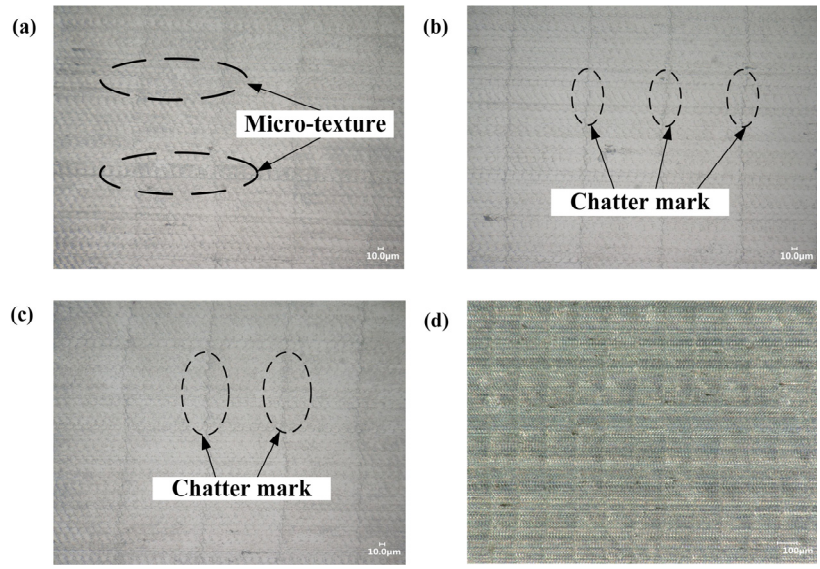


Figure 19. Side milling surface microstructure of LTUM: (**a**–**c**) Surface morphology under high magnification microscope; (**d**) Surface morphology under a low magnification microscope.

Figure 20 shows the surface morphology and surface roughness of side milling (the speed of the main spindle is 1000 r/min, the feed speed is 100 m/min, the radial depth of cutting is 2 mm, and the axial depth of cutting is 5 mm). The surface topography height in the diagram from low to high is blue, green and red. For the same processing parameters, the machined surface was rough and uneven under CM conditions, resulting in irregular gullies and burrs. After longitudinal–torsional ultrasonic vibration was added, the surface morphology of the machined surface changed greatly, and the microstructure formed by

the tool feed could be fairly seen. The reason was that after adding ultrasonic vibration, the trajectory of the tool tip changed from a conventional straight line to an elliptical cutting motion track, which greatly changed the cutting surface. Comparing the surface roughness obtained using the two machining processes methods, the average surface roughness Sa of the workpiece obtained using the CM process was 1.745 μm, while the average surface roughness Sa of the workpiece obtained using LTUM process was 0.418 μm.

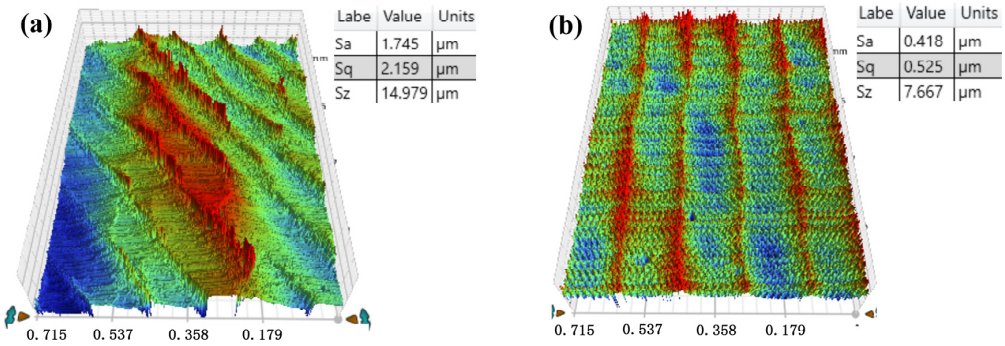


Figure 20. Surface micro-morphology under different side millings: (**a**) CM surface micro-morphology; (**b**) LTUM surface micro-morphology.

Compared with CM, there was an intermittent separation between the LTUM tool and the workpiece, which avoided the abrasion between the flank and the workpiece surface. The abrasion between the tool and the chip was converted to a milling force that was favorable to machining, which reduced the cutting resistance, effectively improved the surface finish of the workpiece, and reduced surface defects. Moreover, ultrasonic vibration imposed a high-frequency pulse impact on the entire processing tool. This pulse impact could soften the surface to be processed, achieve uniform removal of the material, reduce the local deformation of the material in the cutting process, and reduce the roughness of the surface.

Figure 21a shows the surface roughness values of side milling under different radial cutting depths of the two processing methods (the speed of the main spindle is 1000 r/min, the feed speed is 150 m/min). Figure 21b shows the surface roughness value of the two processing methods under different speeds of the main spindle (the feed speed is 150 m/min, the radial cutting depth is 1 mm). Comparing the surface roughness values of the two side milling methods, the surface roughness of LTUM was always smaller than that of CM. The surface roughness value increased with the increase in the radial depth of cutting and decreased with the increase in the speed of the main spindle.

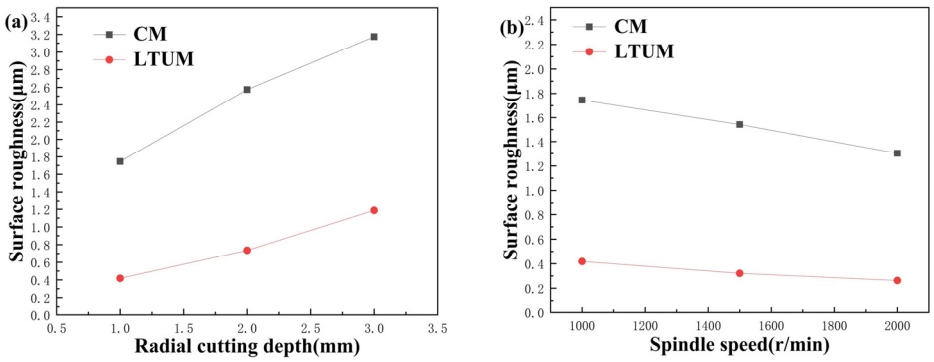


Figure 21. Comparison of roughness values under two processing methods: (**a**) roughness values under different radial cutting depths; (**b**) roughness values at different speeds of the main spindle.

Figure 22 shows the burr morphology of longitudinal–torsional ultrasonic slot milling and traditional slot milling under different cutting depths (the speed of the main spindle is

1000 r/min, the feed speed is 100 m/min). It is not difficult to see that with the increase in the cutting depth, curling burrs appeared in traditional slot milling. When the cutting depth was 1 mm, there were fewer burrs and the burr height was lower; with the increase in slot milling depth, the burr height under both processing methods increased. When the cutting depth reached 3 mm, the number of burrs was the largest and the burr height was the highest. After applying longitudinal–torsional ultrasonic vibration, the number of burrs at the top of the slot side was significantly reduced and the burr height was significantly reduced.

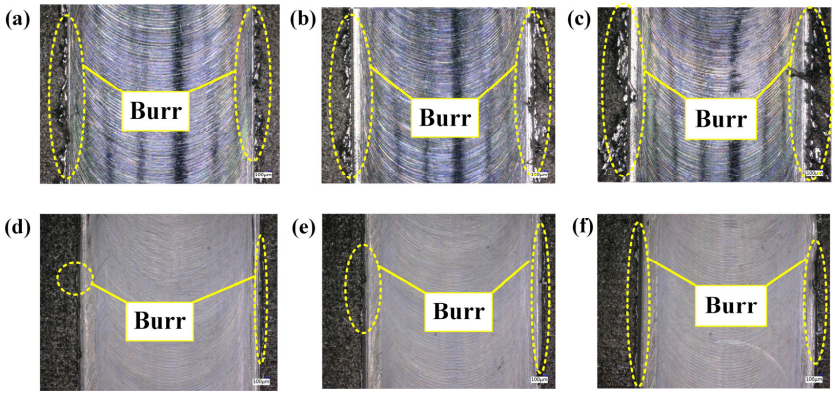


Figure 22. Slot milling surface burr analysis: (**a**) the depth of traditional slot milling is 1 mm; (**b**) the depth of traditional slot milling is 2 mm; (**c**) the depth of traditional slot milling is 3 mm; (**d**) the depth of longitudinal–torsional ultrasonic slot milling is 1 mm; (**e**) the depth of longitudinal–torsional ultrasonic slot milling is 2 mm; (**f**) the depth of longitudinal–torsional ultrasonic slot milling is 3 mm.

Figure 23 shows the micro-topography of the bottom surface of the spindle at different spindle speeds (Figure 23a,d are at a feed rate of 100 m/min and the cutting depth is 1 mm, Figure 23b,e are at a feed rate of 150 m/min and the cutting depth is 1 mm, and Figure 23c,f are at a feed rate of 200 m/min and the cutting depth is 1 mm). Material adhesion occurred on the surface of traditional slot milling, and an irregular texture was generated. With the increase in the speed of the main spindle, the phenomenon of material adhesion gradually increased. After applying longitudinal–torsional ultrasonic vibration, the machined surface formed micro-textured protrusions, and there were basically no defects on the surface. When the speed of the main spindle was 1000 r/min, uniformly spaced textures were generated along the tool feed direction. With the increase in the speed of the main spindle, the number of micro-textures gradually decreased.

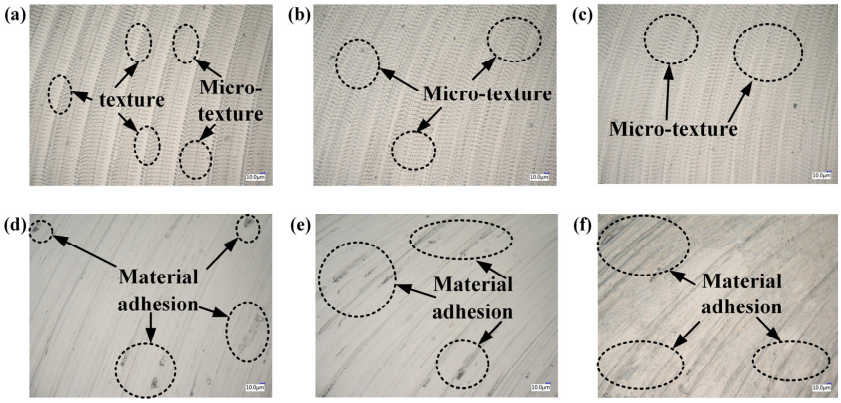


Figure 23. Micro-topography of slot bottom: (**a**) traditional cutting speed of the main spindle is 1000 r/min; (**b**) traditional cutting speed of the main spindle is 1500 r/min; (**c**) traditional cutting speed of the main spindle is 2000 r/min; (**d**) longitudinal–torsional ultrasonic cutting speed of the main spindle is 1000 r/min; (**e**) longitudinal–torsional ultrasonic cutting speed of the main spindle is 1500 r/min; and (**f**) longitudinal–torsional ultrasonic cutting speed of the main spindle is 2000 r/min.

4.3. Effect of LTUM Tool on Cutting Performance

Comparing the milling force changes of the two side milling methods when the speed of the main spindle was 1000 r/min, the feed speed was 100 m/min, the radial cutting depth was 2 mm, and the axial cutting depth was 5 mm, as shown in Figure 24, the standard deviation of the milling force of LTUM was significantly lower than that of CM.

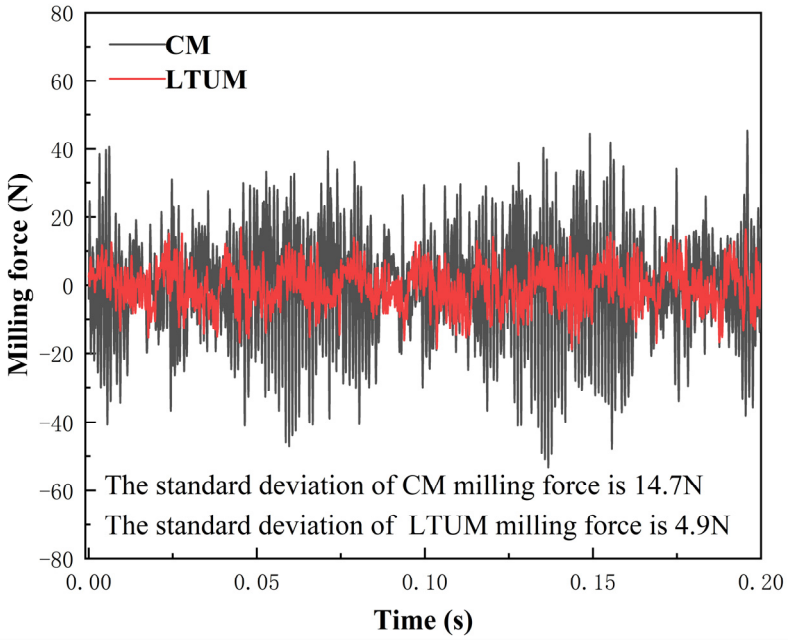


Figure 24. Comparison of the CM and LTUM forces.

This was because of the periodic separation of the tool workpiece with ultrasonic vibration during LTUM, and the actual net cutting time was much smaller than that of CM. It is worth noting that after adding longitudinal–torsional ultrasonic vibration, the milling force was lower than that of CM, which was due to the transformation of the original friction force between the cuttings and the tool into a favorable milling force.

Figure 25a shows the standard deviation of the milling force under two side milling methods under different radial cutting depths (the speed of main spindle is 1000 r/min, the feed speed is 150 m/min). Figure 25b shows the standard deviation of the milling force under two side milling methods under different speeds of the main spindle (the feed speed is 150 m/min, the radial cutting depth is 1 mm). Figure 25c shows the standard deviation of the milling force under two side milling methods under different feeds per tooth (the radial depth of cutting is 1 mm). Figure 25d shows the standard deviation of the milling force under two side milling methods under different feed speeds (the speed of the main spindle is 1000 r/min, radial depth of cutting is 1 mm).

It can be seen from Figure 25 that the milling force of LTUM was always smaller than that of CM, and the milling force did not change much with the feed speed. This was because as the feed speed increased, the removal rate of the workpiece material increased, and the stress of the tool in unit time also increased. However, with the increase in feed speed, the friction coefficient of the rake face of the tool decreased, which slowed down the friction between the tool and the workpiece and reduced the milling force. With the increase in radial cutting depth and feed per tooth, the milling force also increased, and the influence of the radial cutting depth on milling force was greater than that of feed per tooth. With the increase in the speed of the main spindle, the milling force gradually decreased, and the reduction in the milling force generated by CM was greater than that by LTUM. The comparison of the factors affecting the milling force of Inconel 718 was in the order of: radial cutting depth > speed of main spindle > feed per tooth > feed speed.

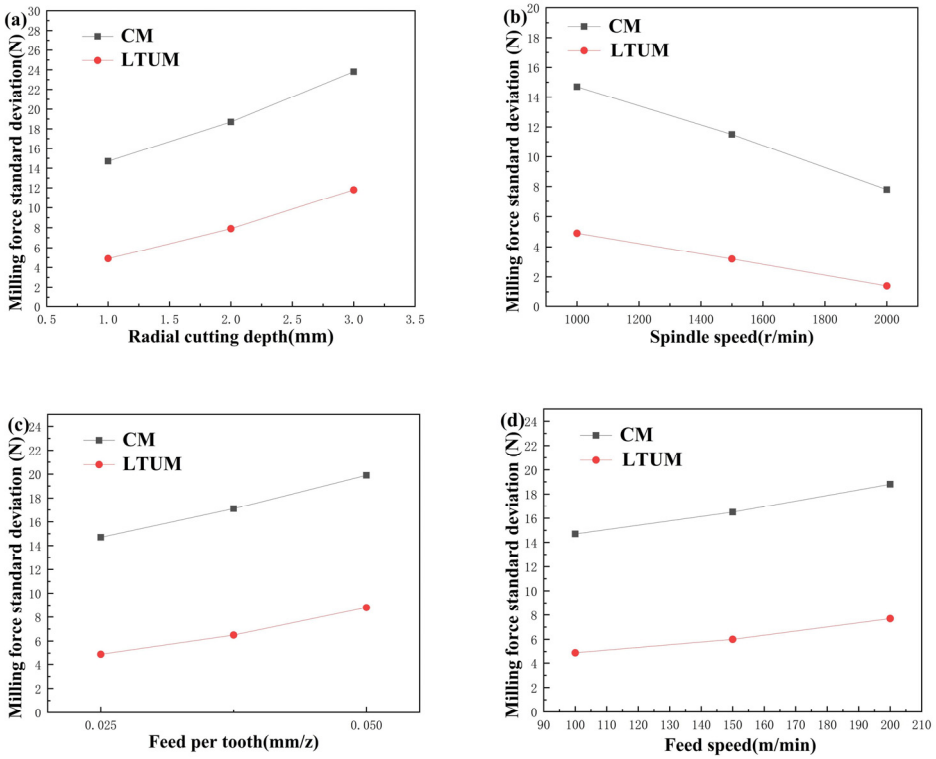


Figure 25. Comparison of the milling forces of two side milling methods under different processing parameters: (**a**) comparison of milling forces under different radial cutting depths; (**b**) comparison of milling forces at different speeds of the main spindle; (**c**) comparison of milling force under different feed per tooth; (**d**) comparison of milling forces at different feed speeds.

The detection equipment used was a VHX-5000 super depth-of-field microscope. Figure 26 shows the flank wear width under two kinds of side milling (the speed of the main spindle is 1000 r/min, the feed speed is 100 m/min, the radial depth of cutting is 2 mm, and the axial depth of cutting is 5 mm). After reading the relevant literature [29–31], it was concluded that the contact conditions on the rake face–chip and flank face–work interfaces could be ignored, and it could be seen that the wear between the tool flank and the workpiece was aggravated under CM processing and the coating on the tool surface was peeled off, resulting in obvious tool wear. This was due to the bonding effect between the material and the tool, and tool flank wear occurred. However, in the LTUM machining method, the flank wear was reduced because the addition of ultrasonic vibration reduced the bond between the tool and the workpiece, reducing the bond wear of the tool.

Figure 27a shows the flank wear width of the two side milling methods under different feed speeds (the speed of main spindle is 1000 r/min, the radial depth of cutting is 1 mm). Figure 27b shows the flank wear width of the two side milling methods under different feeds per tooth (the radial depth of cutting is 1 mm). It can be observed from Figure 27 that with the increase in feed speed and feed per tooth, the flank wear width of the tool increased under both machining methods. Under two different processing parameters, the flank wear width of LTUM was always smaller than that of CM.

The processing parameters were selected as a radial cutting depth of 1 mm, an axial cutting depth of 5 mm, the speed of the main spindle was 1000 r/min, and the side milling chip morphology at the feed speed of 100 m/min. As shown in Figure 28, it can be observed that the chip width generated by LTUM was smaller and more debris was generated, while the chip width obtained by CM was larger and less debris was produced.

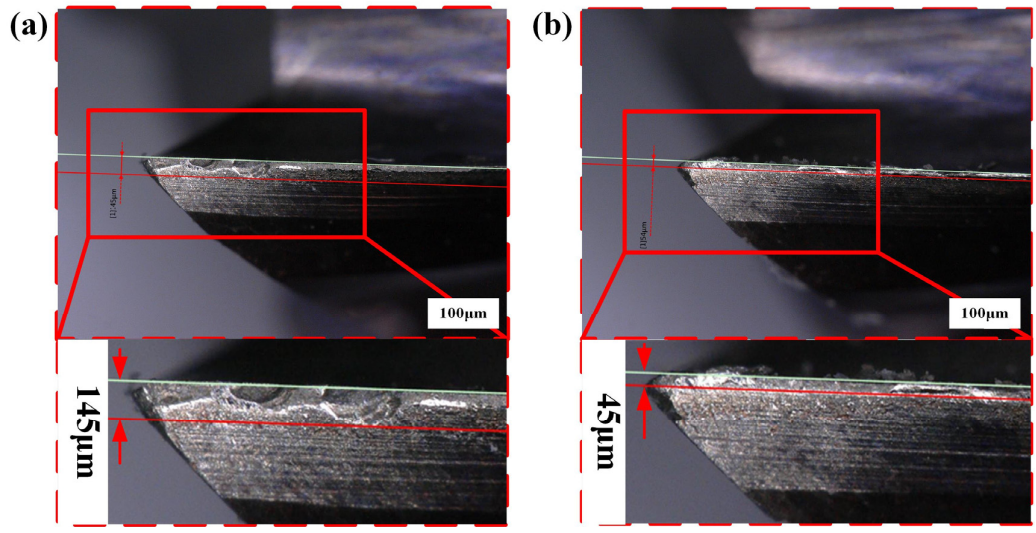


Figure 26. Comparison of tool wear under two side milling processes: (**a**) CM flank wear width; (**b**) LTUM flank wear width.

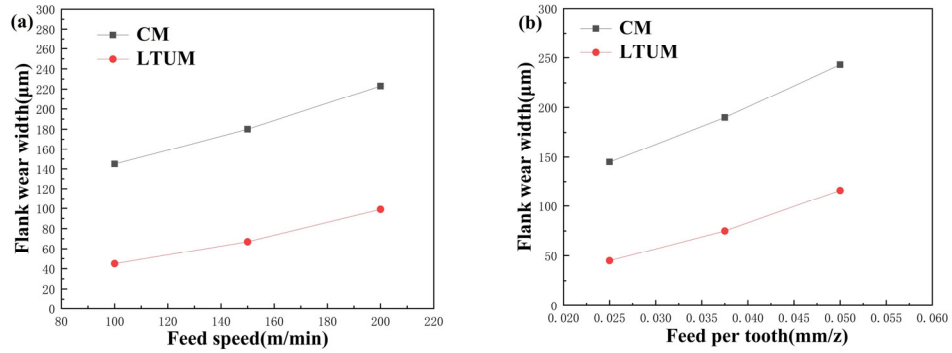


Figure 27. The flank wear width under two side milling methods: (**a**) the flank wear width under different feed speeds; (**b**) the flank wear width under different feed per tooth.

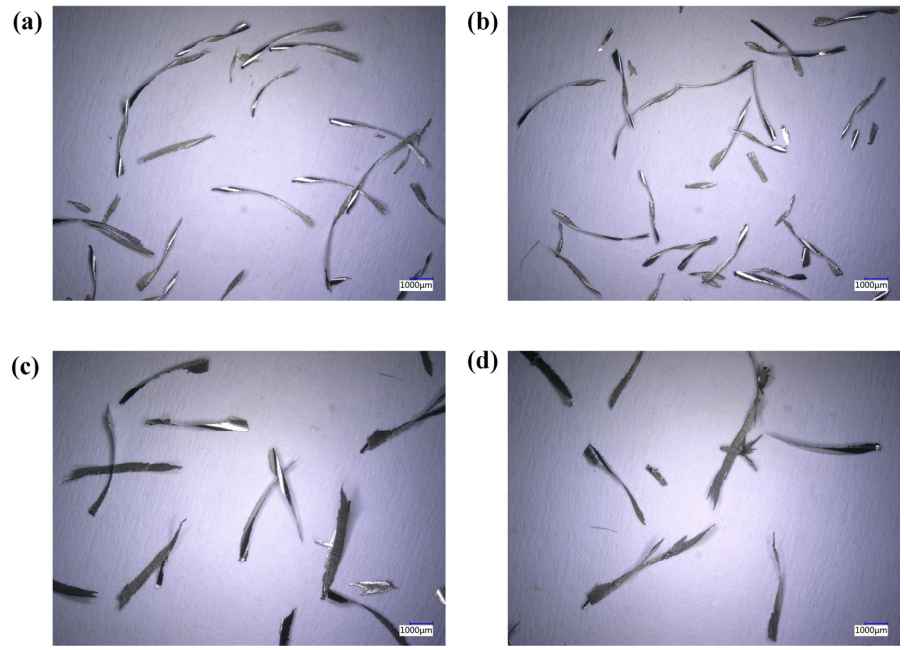


Figure 28. Side milling chip morphology comparison: (**a**,**b**) LTUM chip morphology; (**c**,**d**) CM chip morphology.

5. Conclusions

In this research, an LTUM tool was designed based on previous studies to improve the surface quality and cutting performance of Inconel 718. Based on theoretical computations, finite element simulation and optimization analysis of the tool were conducted, and the LTUM tool was prepared. Performance tests and cutting experiments with the tool were carried out to verify the rationality and cutting performance of the tool, and the following conclusions are drawn:

(1) The LTUM tool was designed based on theoretical computations and finite element analysis. The resonance frequency of the tool is 21.32 kHz, the longitudinal amplitude is 6.8 μm, and the torsional amplitude is 1.4 μm. Transient dynamic analysis of the tool verified that the tool can produce a regular elliptical motion trajectory.

(2) Under side milling, the surface roughness of LTUM is 0.418 μm, which is significantly lower than that of CM, and the surface morphology is obviously improved. Under the two processing methods, the surface roughness value increases with the increase in the radial depth of cutting and decreases with the increase in the speed of the main spindle. Under slot milling, the burr height under LTUM is significantly reduced, which reduces the adhesion of the material on the bottom surface of the slot, and a regular micro-texture is generated at the bottom of the slot, which proves that LTUM can improve the surface quality of Inconel 718.

(3) Compared with CM, the milling force after adding LTUM is significantly reduced. With increases in feed speed, feed per tooth, and radial depth of cutting, the milling force of two kinds of side milling increases, and with the increase in the speed of the main spindle, the milling force of two kinds of side milling decreases. The factors affecting the milling force of Inconel 718 are in the order of: radial cutting depth > speed of main spindle > feed per tooth > feed speed. It is proven that LTUM can improve the cutting performance of Inconel 718.

(4) The flank wear width of the two side milling methods increases with the increase in the speed of the main spindle and feed per tooth. The milling force of LTUM is less than that of CM under the same machining parameters. LTUM processing improves the chip breaking ability, the chip size is small, and more debris is generated.

Author Contributions: Conceptualization, H.Z.; methodology, H.Z.; software, H.Z.; validation, H.Z.; formal analysis, H.Z. and G.S.; investigation, H.Z.; resources, H.Z.; data curation, H.Z.; writing—original draft preparation, H.Z.; writing—review and editing, G.S.; visualization, H.Z.; supervision, G.S., Y.X., P.Z., B.L., Y.S., J.D. and B.F.; project administration, G.S.; funding acquisition, G.S. All authors have read and agreed to the published version of the manuscript.

Funding: This research was funded by [the National Natural Science Foundation of China] [52075275, 51675289], [the Natural Science Foundation of Shandong Province] [ZR2022QE241, ZR2021QE230], [the Talent Research Project of Qilu University of Technology (Shandong Academy of Sciences)] [2023RCKY124], and [the Basic Research Project of Science, Education and Industry Integration Pilot Project of Qilu University of Technology (Shandong Academy of Sciences)] [2022PX044, 2022PY007, 2023PX026, 2023PY021].

Institutional Review Board Statement: Not applicable.

Informed Consent Statement: Not applicable.

Data Availability Statement: The original contributions presented in the study are included in the article, further inquiries can be directed to the corresponding author.

Conflicts of Interest: The authors declare no conflicts of interest.

References

1. Ma, Z.; Xu, X.; Huang, X.; Ming, W.; An, Q.; Chen, M. Cutting performance and tool wear of SiAlON and TiC-whisker-reinforced Si_3N_4 ceramic tools in side milling Inconel 718. *Ceram. Int.* **2022**, *48*, 3096–3108. [CrossRef]
2. Wang, H.; Pei, Z.J.; Cong, W.L. A feeding-directional cutting load model for end surface grinding of CFRP composites using rotary ultrasonic machining with elliptical ultrasonic vibration. *Int. J. Mach. Tools Manuf.* **2020**, *152*, 103540. [CrossRef]

3. Zhao, B.; Chang, B.Q.; Wang, X.B. System design and experimental research on ultrasonic assisted elliptical vibration grinding of Nano-ZrO_2 ceramics. *Ceram. Int.* **2019**, *45*, 24865–24877. [CrossRef]
4. Lotfi, M.; Amini, S.; Aghayar, Z.; Sajjady, S.A.; Farid, A.A. Effect of 3D elliptical ultrasonic assisted boring on surface integrity. *Measurement* **2020**, *163*, 108008. [CrossRef]
5. Lan, S.L.; Qi, M.; Zhu, Y.F.; Liu, M.X.; Bie, W.B. Ultrasonic rolling strengthening effect on the bending fatigue behavior of 12Cr2Ni4A steel gears. *Eng. Fract. Mech.* **2023**, *279*, 109024. [CrossRef]
6. Ao, N.; Liu, D.X.; Zhang, X.H.; Wu, S.C. Improved fretting fatigue mechanism of surface-strengthened Ti-6Al-4V alloy induced by ultrasonic surface rolling process. *Int. J. Fatigue* **2023**, *170*, 107567. [CrossRef]
7. Xie, W.; Wang, X.K.; Zhao, B.; Li, G.X.; Xie, Z.J. Surface and subsurface analysis of TC18 titanium alloy subject to longitudinal-torsional ultrasonic vibration-assisted end milling. *J. Alloys Compd.* **2022**, *929*, 167259. [CrossRef]
8. Kuo, K.-L. Ultrasonic vibrating system design and tool analysis. *Trans. Nonferrous Met. Soc. China* **2009**, *19*, s225–s231. [CrossRef]
9. Li, Y.; Yang, Y.; Wang, Y.; Gao, F. Study on the simulativeand experiment of ultrasonic-assisted vibration drilling of Ti6Al4V. *J. Phys. Conf. Ser.* **2022**, *2242*, 012011. [CrossRef]
10. Li, Z.C.; Jiao, Y.; Deines, T.W.; Pei, Z.J.; Treadwell, C. Rotary ultrasonic machining of ceramic matrix composites: Feasibility study and designed experiments. *Int. J. Mach. Tools Manuf.* **2005**, *45*, 1402–1411. [CrossRef]
11. Di Iorio, E.; Bertolini, R.; Bruschi, S.; Ghiotti, A. Design and development of an ultrasonic vibration assisted turning system for machining bioabsorbable magnesium alloys. *Procedia CIRP* **2018**, *77*, 324–327. [CrossRef]
12. Xie, Z.W.; Liu, Z.Q.; Han, L.C.; Wang, B.; Xin, M.Z.; Cai, Y.K.; Song, Q.H. Optimizing amplitude to improve machined surface quality in longitudinal ultrasonic vibration-assisted side milling 2.5 DC/SiC composites. *Compos. Struct.* **2022**, *297*, 115963. [CrossRef]
13. Namlu, R.H.; Yılmaz, O.D.; Lotfisadigh, B.; Kılıç, S.E. An experimental study on surface quality of Al6061-T6 in ultrasonic vibration-assisted milling with minimum quantity lubrication. *Procedia CIRP* **2022**, *108*, 311–316. [CrossRef]
14. Wang, Z.Y.; He, Y.J.; Yu, T.B. Surface quality and milling force of SiCp/Al ceramic for ultrasonic vibration-assisted milling. *Ceram. Int.* **2022**, *48*, 33819–33834. [CrossRef]
15. Qin, S.Q.; Zhu, L.; Wiercigroch, M.; Ren, T.Y.; Hao, Y.P.; Ning, J.S.; Zhao, J. Material removal and surface generation in longitudinal-torsional ultrasonic assisted milling. *Int. J. Mech. Sci.* **2022**, *227*, 107375. [CrossRef]
16. Yin, X.M.; Liu, Y.H.; Zhao, S.C.; Li, X.; Geng, D.X.; Zhang, D.Y. Tool wear and its effect on the surface integrity and fatigue behavior in high-speed ultrasonic peening milling of Inconel 718. *Tribol. Int.* **2023**, *178*, 108070. [CrossRef]
17. Ni, C.B.; Zhu, L.D.; Liu, C.F.; Yang, Z.C. Analytical modeling of tool-workpiece contact rate and experimental study in ultrasonic vibration-assisted milling of Ti–6Al–4V. *Int. J. Mech. Sci.* **2018**, *142*, 97–111. [CrossRef]
18. Chen, G.; Zou, Y.H.; Qin, X.D.; Liu, J.; Feng, Q.; Ren, C.Z. Geometrical texture and surface integrity in helical milling and ultrasonic vibration helical milling of Ti-6Al-4V alloy. *J. Mater. Process. Technol.* **2020**, *278*, 116494. [CrossRef]
19. Chang, B.Q.; Yi, Z.X.; Cao, X.B.; Duan, J.A. Defect suppression and grain refinement during ultrasonic vibration-assisted side milling of GH4169 superalloy. *J. Manuf. Process.* **2023**, *85*, 281–294. [CrossRef]
20. Long, Z.L.; Liu, Y.C.; Zhang, Z.Y.; Liu, S.; Zhou, J.J. Design for torsional transducer in ultrasonic machining based on equivalent circuit. In Proceedings of the 2017 IEEE International Conference on Information and Automation (ICIA), Macao, China, 18–20 July 2017; pp. 953–958.
21. Ma, Y.J.; Nie, W.Z.; Lu, J.M.; Chen, H. Study on surface quality of BK7 optical glass by longitudinal torsional composite ultrasonic vibration milling. *Mater. Sci. Forum* **2020**, *984*, 51–57. [CrossRef]
22. Ying, N.; Feng, J.; Bo, Z.; Guo, F.G.; Jing, J.N. Theoretical investigation of machining-induced residual stresses in longitudinal torsional ultrasonic–assisted milling. *Int. J. Adv. Manuf. Technol.* **2020**, *108*, 3689–3705. [CrossRef]
23. Geng, D.X.; Zhang, D.Y.; Xu, Y.G.; He, F.T.; Liu, D.P.; Duan, Z.H. Rotary ultrasonic elliptical machining for side milling of CFRP: Tool performance and surface integrity. *Ultrasonics* **2015**, *59*, 128–137. [CrossRef] [PubMed]
24. Zheng, Z.P.; Zhang, J.F.; Feng, P.F.; Wang, J.J. Controllable fabrication of microstructures on the metallic surface using oblique rotary ultrasonic milling. *Int. J. Mech. Sci.* **2023**, *237*, 107805. [CrossRef]
25. Du, P.F.; Han, L.; Qiu, X.; Chen, W.S.; Deng, J.; Liu, Y.X.; Zhang, J.J. Development of a high-precision piezoelectric ultrasonic milling tool using longitudinal-bending hybrid transducer. *Int. J. Mech. Sci.* **2022**, *222*, 107239. [CrossRef]
26. Wang, D.A.; Chuang, W.Y.; Hsu, K.; Pham, H.T. Design of a Bézier-profile horn for high displacement amplification. *Ultrasonics* **2011**, *51*, 148–156. [CrossRef] [PubMed]
27. Yin, S.; Dong, Z.G.; Bao, Y.; Kang, R.K.; Du, W.H.; Pan, Y.N. Development and optimization of ultrasonic elliptical vibration cutting device based on single excitation. *J. Manuf. Sci. Eng.* **2021**, *143*, 081005. [CrossRef]
28. Mughal, K.H.; Qureshi, M.A.M.; Raza, S.F. Novel ultrasonic horn design for machining advanced brittle composites: A step forward towards green and sustainable manufacturing. *Environ. Technol. Innov.* **2021**, *23*, 101652. [CrossRef]
29. Liu, Y.; Geng, D.; Zhang, D.; Zhai, Y.; Liu, L.; Sun, Z.; Shao, Z.; Zhang, M.; Jiang, X. Cutting performance and surface integrity for rotary ultrasonic elliptical milling of Inconel 718 with the ball end milling cutter. *J. Mater. Process. Technol.* **2023**, *319*, 118094. [CrossRef]

30. Gao, G.; Xia, Z.; Su, T.; Xiang, D.; Zhao, B. Cutting force model of longitudinal-torsional ultrasonic-assisted milling Ti-6Al-4V based on tool flank wear. *J. Mater. Process. Technol.* **2021**, *291*, 117042. [CrossRef]
31. Chen, P.; Tong, J.; Zhao, J.; Zhang, Z.; Zhao, B. A study ofthe surface microstructure and tool wear of titanium alloys after ultrasonic longitudinal-torsional milling. *J. Manuf. Process.* **2020**, *53*, 1–11. [CrossRef]

Disclaimer/Publisher's Note: The statements, opinions and data contained in all publications are solely those of the individual author(s) and contributor(s) and not of MDPI and/or the editor(s). MDPI and/or the editor(s) disclaim responsibility for any injury to people or property resulting from any ideas, methods, instructions or products referred to in the content.